UC Irvine
UC Irvine Previously Published Works

Title

The Effects of Dynamic Dispatch on the Degradation and Lifetime of Solid Oxide Fuel Cell Systems

Authors

Nakajo, Arata
Mueller, Fabian
McLarty, Dustin
et al.

Peer reviewed

The Effects of Dynamic Dispatch on the Degradation and Lifetime of Solid Oxide Fuel Cell Systems

A. Nakajo,[a,z] F. Mueller,[b] D. McLarty,[b] J. Brouwer,[b] J. Van herle,[a] and D. Favrat[a]

[a]*Laboratoire d'Energétique Industrielle, Institut de Génie Mécanique, Ecole Polytechnique Fédérale de Lausanne, Switzerland*
[b]*National Fuel Cell Research Center, University of California, Irvine, California, USA*

Understanding of mechanisms affecting degradation, durability and performance of solid oxide fuel cell (SOFC) stacks and integrated systems has become important due to increasing worldwide deployment. A novel simulation approach accounting for state-of-the-art understanding of degradation mechanisms in the context of an operating SOFC system has been developed. Investigative tools simulating lifetime degradation have been applied to a physical SOFC system model designed and controlled to allow dynamic dispatch. The system was operated in two modes (a) constant power output mode, and (b) diurnal dynamic dispatch mode. Results show that on a time basis the dynamically dispatched SOFC system proved more durable and degraded less than a system operated at constant full-power output. The net energy production over the stack lifetime was roughly equivalent between the two modes (1.5 to 2 kWh cm^{-2}), with the dynamically dispatched fuel cell operating longer, degrading less and producing more power during highly valued peak demand periods.
© 2011 The Electrochemical Society. [DOI: 10.1149/2.032111jes] All rights reserved.

The solid oxide fuel cell (SOFC) is a direct energy conversion technology that provides decisive advantages in terms of efficiency, fuel flexibility and load following capabilities. The current state-of-the-art lacks the durability expected by industry and public utilities, limiting heavily market penetration. The lack of complete understanding of degradation processes that affect performance and mechanical reliability have resulted in conservative operation strategies that hinder the potential effectiveness and benefit of SOFC devices. First-generation commercial products are just now being deployed for large field tests by several major manufacturers. These manufacturers and system operators must consider the possibility of a value-added benefit from additional operational strategies including transient dispatch modes.

Several known degradation mechanisms exist that reduce SOFC performance, often depending upon stack design, system implementation and operating conditions. They arise from instabilities of the materials in the harsh reduction and oxidation environments, volatile contaminating species in the feed gases, and uneven distribution of local conditions. Cathodes made of lanthanum strontium manganite and yttria-stabilized zirconia (LSM-YSZ) composite or of single-component lanthanum strontium cobaltite ferrite (LSCF) are subjected to chromium contamination and formation of lanthanum (LZO) or strontium zirconate (SZO) phases with low electrical conductivity.[1–6] Nickel-based (Ni-YSZ) anodes suffer from sulfur poisoning, nickel particle coarsening and re-oxidation.[7,8] The ohmic losses increase in a SOFC stack due to the oxidation of the metallic interconnects (MIC) and decrease of the ionic conductivity of YSZ.[9,10]

The understanding of mechanical failures of SOFC stacks, which in practice quickly lead to their end of life, is incomplete. Proper stack design and operating strategies are crucial to guarantee the structural integrity of the components. Cell cracking can arise from (i) the residual stress inherent to the multilayer nature of the cell,[11–13] (ii) thermal stress induced by the uneven temperature distribution in operation[14,15] (iii) mechanical interactions with the other stack components, and indirectly from (iv) loss of gas-tightness and electrical contact, through a succession of detrimental alterations.[16,31] Improper control during following of the electrical power demand drastically increases the risks of failure.[16] The use of glass-ceramic sealants requires particular care.[17,31] In the long-term, creep and weakening of the materials that may ensue physico-chemical alterations can activate additional failure

modes.[12,31] In this view, spatial temperature control is of interest to ensure safe conditions during transients and mitigate the detrimental effects of irreversible deformation generated in operation.[18]

Analyses and characterization of SOFC materials performance and degradation must be integrated with the analyses of the complete system within which the SOFC operates. The electrical, mass flow and thermal integration of the stack with the remaining balance of plant (BoP) induces several constraints and compounding factors that may alleviate or amplify the severity of the degradation mechanisms. In the present study, a previously developed system level modeling methodology has been expanded and utilized in conjunction with the stack degradation analysis to demonstrate the lifetime impact of dispatched operation. The methodology has previously been used to simulate stand alone high temperature fuel cell configurations and advanced concepts such as the fuel cell gas turbine hybrid.[19–26]

The modeling methodology discretizes each system component into multiple control volumes that separate the basic physics and allow for spatial determination of local conditions such as temperature, pressure, and concentration. Dynamic conservation expressions for mass, energy, and composition are evaluated simultaneously with expressions for transport phenomena (e.g. heat transfer and diffusion), chemical reaction kinetics (e.g. reforming and water-gas shift) and a robust electrochemical model. Individual component models can be integrated into complex system models in a variety of configurations, including combined cooling, heat and power applications, upon which the design of various control strategies can be implemented and tested.[27–30]

The aim of the present study is to show how (i) a SOFC system can be adequately designed and controlled in the view of dispatched electrical power generation, with (ii) a minimal penalty or even positive impact on the lifetime of the device, and in particular with beneficial economic implications. Several distinct models have been developed for (i) SOFC system design and control synthesis[19–30] and (ii) analysis and mitigation of the electrochemical degradation at the stack scale.[31–33] These models constitute the basis for the analysis. The combination of these different aspects is required for the present purpose to correctly capture the complexity of the issues and understand the underlying physics. To our knowledge, it is the first time that an approach that retrieves knowledge from the electrode micro-scale to the system macro-scale is applied on the analysis of the short- and long-term dynamic analysis of a SOFC system. The simulations compare two different operating modes of the SOFC system: (i) constant power output and (ii) diurnal dynamic dispatch. The feasibility is first

demonstrated at the system level. Then, the impact of the operating mode on the degradation behavior of the SOFC stack is investigated and characterized.

Model Development

System Level Analysis Model Description.— Control design and system analyses were accomplished using detailed first principles models developed in the MatLab-Simulink® framework. The simulated system employs a spatially- and temporally-resolved fuel cell model that accounts for internal manifolding heat transfer using simplified planar flow geometry. Additional bulk and nodal dynamic models account for the remaining balance of plant components to simulate a complete SOFC system operating with an external reformer.[21] The case of cathode-supported cell is considered here, like for previous system studies.[19,21–26,28–30] For degradation profiles, the modeling framework developed for anode supported stack technology[15,16,31–33] was implemented. Though the temperature profile in an anode-supported cell may differ, system controls will respond identically to either design, since the main outcome of the stack system model is to determine a voltage loss.

System level analysis - Integrated Stack/Manifold.— The quasi-3D dynamic model simulates a generic planar SOFC design with scalable active area and the option for internal and/or external reforming. Discretization of the cell cross-section into 25 nodes provides a good balance between computational efficiency and accuracy. Five distinct control volumes comprise each node; oxidant separator plate (interconnect), cathode gas, membrane electrode assembly (MEA), anode gas, and fuel separator plate (interconnect). Spatial resolution allows for analyses of internal temperature profiles, and thus internal heat transfer must be modeled with precision. This approach provides significant improvement in accuracy over a bulk model, particularly in the tasks of system design, scaling and control, while accurately determining SOFC performance within the system. The primary dynamic expressions for mass flow, temperature, and species conservation assume a perfectly stirred reactor for each gaseous control volume, an equipotential electrode, and ideal gas behavior for mass flow and convective heat transfer. The thermal balance relies upon seven parameter curve fits for the specific heat capacities of each of the seven species considered; CH_4, CO, CO_2, H_2, H_2O, N_2, O_2. Representative dynamic expressions of the model are as follows for species, temperature and pressure:

$$\frac{R_{Ref+Consume} + (\dot{n} \cdot X_i)_{in-out}}{P \forall / R_U T} = \frac{dX_i}{dt} \quad [1]$$

$$\frac{\sum Q_i + \dot{q}}{C_p m} = \frac{dT}{dt} \quad [2]$$

$$\frac{(\dot{n}_{in} - \dot{n}_{out}) \cdot R_u \cdot T}{\forall} = \frac{dP}{dt} \quad [3]$$

The electrochemical model accounts for general overpotential characteristics at the electrode/electrolyte interfaces including both activation and diffusion polarization losses. The model was tuned to state-of-the-art data with the constant values in Table I.

$$\eta_{cath} = \frac{R_U T}{4F} ln \frac{j * c_R^*}{j_L * c_R^0} \quad [4]$$

$$\frac{c_R^*}{c_R^0} = \frac{1}{P^C \left\{ x_{O_2|d} - t^C jRT / \left(4FP^C D_{O_2,N_2}^{eff} \right) \right\}} \quad [5]$$

$$\eta_{ohm} = j \frac{t^M T}{K e^{-\Delta G_{act}/(RT)}} \quad [6]$$

Table I. Electrochemical overpotential parameters.

Property	Symbol	Value	Units
Effective Oxygen Diffusivity	D_{O_2,N_2}^{eff}	2×10^{-5}	(m^2/s)
Transfer Coefficient	α	0.7	(none)
Exchange Current Density	j_0	1	(A/cm^2)
Electrolyte	K	13×10^7	$(K/(\Omega \cdot m))$
Electrolyte Activation Energy	ΔG_{act}	100	(kJ/mol)
Electrolyte Thickness	t_m	18	μm
Anode Thickness	t_{an}	50	μm
Cathode Thickness	t_{cath}	800	μm

The current work extends previous methodologies through integration of pre- and post-heating manifolds into the stack configuration. This novel approach captures the physics that couples internal manifolding to cell performance characteristics and temperature distributions within a fuel cell stack. This is achieved through the description of a simplified manifolding geometry wherein the incoming air and fuel streams flow pass the stack edges prior to entering the active cell area and after exiting the active cell area.

System level analysis - Balance of Plant.— The additional components considered in the system design are an external reformer, air and fuel pre-heaters, post combustor, blower and bypass valves, which are arranged as shown in Figure 1. Both the nodal heat exchanger models and nodal reformer model utilize the same dynamic expressions for energy and mass conservation. The chemical kinetics for methane reformation with steam applied in the reformer model utilize reformation equations and rate constants determined by Xu and Froment.[34] The oxidizer assumes complete combustion of any remaining methane, carbon monoxide, and hydrogen in a perfectly stirred reactor volume with the previous control volume analysis for mass conservation and pressure. The parasitic load of the blower is subtracted from the electrical production of the fuel cell to determine the net system power.

$$\dot{W}_{Net} = \dot{W}_{FC} - \dot{W}_{Blower} \quad [7]$$

System level analysis - Control Design.— The SOFC system with external reforming requires control of sufficient system actuators to manipulate electrical power output, fuel utilization, cathode inlet temperature, and cathode exhaust temperature within desired limits. The control scheme applied uses six feedback loops to meet varying power demand while maintaining operating conditions within desired limits. Each measurement signal is normalized by its design value and the resulting feedback passes through a traditional PI controller for the appropriate actuator. Some actuators, such as fuel supply, rely solely on feed-forward control. Electronic current controls use feedback from measured power to manipulate stack voltage. Electric current measurements and a desired fuel utilization provide the feed-forward control for the natural gas supply. Stack inlet temperature, maintained at a fixed set-point or at a variable look-up table value, relies upon manipulation of a recouperator bypass valve to divert hot cathode
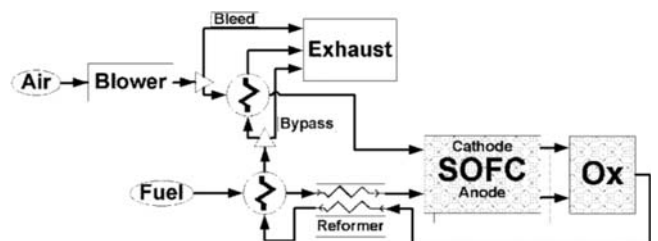
Figure 1. Externally reformed SOFC system diagram.

Table II. Control system design specification.

System Parameter	Manipulated Variable	Control Values	
		P	I
Power	Voltage	1e-2	2e-1
Fuel Use	Fuel Flow	Feed-Forward	
FC Inlet Temp	Bypass Valve	0.02	1e-5
FC Inlet Temp	Oxidizer Fuel	0	1e-5
FC Outlet Temp	Blower Power	0.02	5e-6
FC Outlet Temp	Bleed Valve	0.01	5e-6

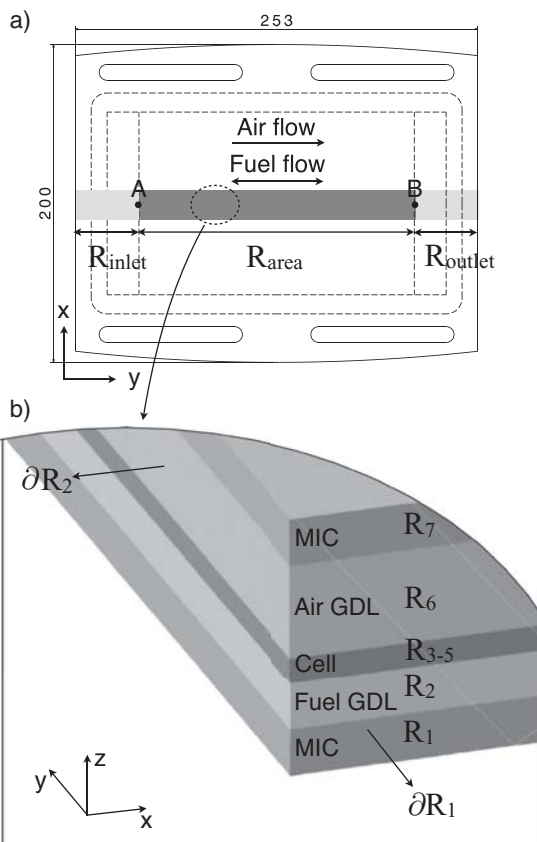

Figure 2. FlameSOFC project SRU design.

exhaust around the pre-heater to cool the inlet, and/or additional fuel injection to the oxidizer to increase the inlet temperature. The measured inlet temperature dictates the bypass valve position, and once valve position saturates in the closed position the inlet temperature measurement dictates the amount of additional fuel supplied to the post-fuel cell oxidizer. Cathode exhaust temperature is controlled via the air flow rate by manipulating the amount of power supplied to the blower unit. Upon reaching the lower saturation limit of the blower, a bleed valve diverts air from the fuel cell inlet to the exhaust, thereby bypassing the fuel cell entirely in low power operation.

The overall system control strategy is presented in Table II with the proportional and integral (PI) control gains for each feedback loop. Note the smaller control values for measurements of fuel cell outlet conditions due to the slower response caused by the large gaseous volume and thermal mass between actuator and measurement. Previous dynamic modeling has demonstrated the distinct ranges of the relevant time scales for electrochemical, fluid dynamic and thermal transport processes.[35] Thus the control gain setting for power, 1e-2, causes changes in <1s while a much smaller gain for inlet temperature, 1e-5, affects the system in >100s. The inlet temperature responds much quicker than cathode outlet temperature to system perturbations such as changing air flow rates and bypass valve position and therefore inlet actuators are constrained tighter. Oxidizer fuel injection and blower bleed valve are triggered feedback loops only active when saturation is reached for the bypass valve and blower power respectively.

Degradation and Lifetime Analysis Model Description.— The degradation and lifetime analyses were conducted using a 2.5 kWe SOFC stack design, based upon anode-supported cells, developed within the FP6 European FlameSOFC project, for combined heat and power application.[31,43] The one-dimensional single-repeated-unit (SRU) model is implemented in gPROMS, an equation-oriented process modeling tool.[36] Figure 2 depicts the actual geometry of the FlameSOFC SRU, and the simplification to three sub-domains, i.e. electrochemically-active (R_{active}), air entry (R_{inlet}) and exhaust (R_{outlet}) zones. The electrochemical model is based on physical principles, which enables the implementation of degradation phenomena.

Lifetime analysis - Electrochemical Model[32].— Ohmic losses comprise the ionic resistivity of the electrolyte, corrected for constriction effects, the electronic resistivity of the MIC, its oxide layer and contact resistance, and a limited electronic conductivity of the electrolyte that induces a small leakage current. The case of LSM-YSZ cathode is considered. The expression for the transfer current holds for the sequence of elementary processes proposed by van Heuveln et al.[37] The dusty-gas model and continuity are solved for the anode supported cell. The approach of Achenbach et al. accounts for reforming and the water-gas shift Achenbach et al.[38] Only hydrogen is electrochemically converted at the interface, as proposed by Zhu et al.[39] The model has been calibrated against data from two segmented-cell experiments.[32]
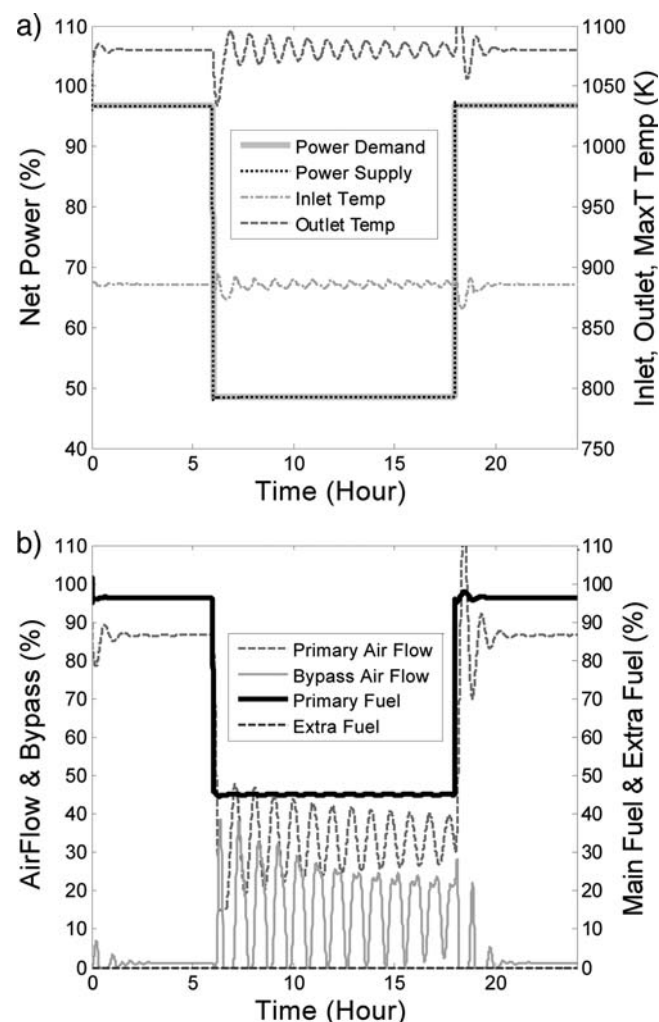
Lifetime analysis - Degradation Phenomena[33].— Five degradation phenomena are modeled. *(i)* An empirical model reproduces the experimental data on the decrease of the ionic conductivity of 8YSZ

during aging in air and is used to predict the increase in resistance of both the electrolyte and the 8YSZ phase in the LSM-YSZ cathode. *(ii)* Sufficient experimental data for accurate prediction of corrosion on coated MIC does not exist, therefore temperature dependence and gas composition dependence is assumed identical to uncoated MIC.[40] However, to limit oxide scale growth to the practical case of a coated MIC, i.e. $Mn_{1.5}Co_{1.5}O_4$, the rate is adapted to match the relation by Liu et al.[41] at 1073 K. *(iii)* A percolation model[33] predicts the reduction of the triple-phase boundary (TPB) due to the growth of nickel particles in the anode. The semi-empirical relation for the evolution of the nickel particle radius depends on temperature, steam and hydrogen partial pressure and tends to a maximum value due to the mechanical constraint imposed by the YSZ network.[33] *(iv)* Chromium contamination for a LSM-YSZ cathode assumes progressive blocking of active sites by electrochemically-deposited Cr_2O_3 from $CrO_2(OH)_2(g)$ released by the MIC. The local overpotential governs the deposition process within the composite cathode, which depends on the steam and $CrO_2(OH)_2(g)$ partial pressures. A typical compressed air steam content of 0.1% is assumed.[5] The gaseous $CrO_2(OH)_2$ content is governed by mass transport limitations, as suggested by Opila et al.[42,43] The equilibrium partial pressures for all chromium species are computed from thermodynamic data produced by Ebbinghaus et al.[44] for a Cr_2O_3 oxide. The modeling here of a Cr_2O_3 MIC oxide scale yields excessive predictions for chromium contamination since coatings reduce the release of chromium volatile species.[45,46] *(v)* Electrically-insulating LZO/SZO phases cause severe detrimental effects on LSM-YSZ cathode performance.[5] A lack of quantitative data inhibits detailed modeling, but sufficient data exist to enable prediction of the onset of formation. The thermodynamic data on the critical oxygen partial pressure from Liu et al.[6] is interpolated and compared with the local one, computed from the local overpotential in the LSM-YSZ cathode and oxygen gas phase concentration.

Results

System Analyses.— The goal of the current work is to determine: (a) whether or not one can design and control a SOFC system to operate in a peaking mode to increase revenue by producing more power at higher valued times, and (b) whether electrochemical degradation of the SOFC may be adversely affected by dynamic dispatch of the SOFC in such a peaking mode. As a result, the simulated SOFC system was cycled between full-load (between noon and 8:00 PM each day) and half-load (the remainder of the day) for a period of several days. The system turn-down from full- to half-power and ramp-up from half- to full-power were each performed in one minute, demonstrating a rapid response to demand changes while maintaining a satisfactory internal SOFC temperature profile. The controlled SOFC system demonstrated robust ability to meet a variety of set points for cathode inlet and exhaust temperatures during such extreme transient operation. Slow actuator response led to a resonance phenomenon as thermal energy oscillated between the mass of the FC stack, the external reformer and the air pre-heat heat exchanger masses. Stronger control of the manipulated variables ensured nominal operating conditions for the stack during steady operation. A prediction of spatial temperature profiles shows minimal thermal gradient changes during the transient periods simulated. System level responses are shown in Figure 3 and Figure 4. Note that the SOFC dynamic simulation suggests that one can moderate the fuel cell inlet perturbations to achieve relatively constant performance during rapid and extreme transient operation associated with dynamic dispatch and changes in ambient conditions.

Figure 3 shows a thermal response in which the stack inlet and exhaust temperature fluctuate 180° out of phase. The sudden decrease to half power, occurring at 6 hours, reduces internal heating, cathode outlet temperature quickly drops, triggering a reduction in cathode airflow. Simultaneously, the average temperature gradient decreases, lowering voltage and increasing current. Additional fuel maintains fuel utilization, and coupled with the reduced air flow, oxidizer outlet temperature increases, thereby raising recouperator effectiveness. The result is higher inlet temperatures, despite a dropping cathode outlet temperature. In a poorly designed controller, like that shown in Figure 3, the thermal response of the stack operates on the same time scale as the recouperator bypass valve, thus producing undesired harmonics. The opposite chain of events occurs during a ramp-up from half- to full-power, though the harmonics subside much quicker.

System control with calibrated control parameters demonstrates the ability to keep system operating limits within design constraints. Figure 4 shows a system response to the same dispatched operation with minimal undesired transient response. The system electrical output can easily ramp from half- to full-load in one minute. However, the thermal response is much slower due to the large mass of the fuel cell. Calibration of the control strategy eliminates thermal oscillations and peak MEA temperature is held within constraints for both full- to half-load and half- to full-load transients. The temperature gradient across the stack remains within 15 K of nominal operation throughout the transient behavior. Figure 4 demonstrates how the thermal mass of the fuel cell buffers the change in inlet conditions. For the half to full lad transient (zoom in Figure 4c and 4d), fuel is quickly added to the reformer, causing the sudden drop in cathode inlet temperature. The endothermic reactions of the external reformer cool the exhaust stream and reduce the effectiveness of the recouperator, thereby cooling the cathode inlet stream. Additional fuel, approximately 10% of the nominal fuel flow rate, is supplied to the oxidizer and provides additional heat to the exhaust upstream of the reformer and recouperator. The additional enthalpy from combusting extra fuel is needed for 20 to 25 minutes to minimize inlet temperature fluctuation as the system ramps up to full-load. The cathode exhaust and MEA peak temperature, both indicators of the internal temperature profile, are minimally affected as the system returns to nominal inlet conditions.

Stack Analyses.— The stack performance was investigated under the two operating modes; fixed and cyclic. Under fixed load operation, the specific power was held constant at either 0.28 W/cm^2 or 0.14 W/cm^2. The cyclic operation cycled the specific power between 0.28 W/cm^2 (full load) and 0.14 W/cm^2 (half load). The stack performed at the higher specific power from noon to 8:00 PM, and the lower specific power for the remaining 16 hours each day. Furthermore the cyclic operation was constrained in one of four ways; (a) Fixed stack inlet temperature, maximum MEA temperature, and fuel utilization; or, minimized temperature profile change between full and half load using: (b) Variable stack inlet temperature, (c) Variable stack inlet temperature and maximum MEA temperature, (d) Variable stack inlet temperature and fuel utilization (up to 90%).

Figure 3. a) 24 hour thermal response to dynamic dispatch with weak feedback controllers. b) Associated control perturbation.

Table III. Test case nomenclature specification. (a) Fixed stack inlet temperature, maximum MEA temperature, and fuel utilization. Strategies minimizing temperature profile change between full and part load: (b) variable stack inlet temperature, (c) variable stack inlet temperature and maximum MEA temperature and (d) variable stack inlet temperature and fuel utilization (up to 90%).

Parameter Name	Initial
Fixed Power or Cyclic Power	P or CP
Power Density 0.28 or 0.14 W/cm^2	28/14
Constraint Method a), b), c), or d)	a, b, c, d
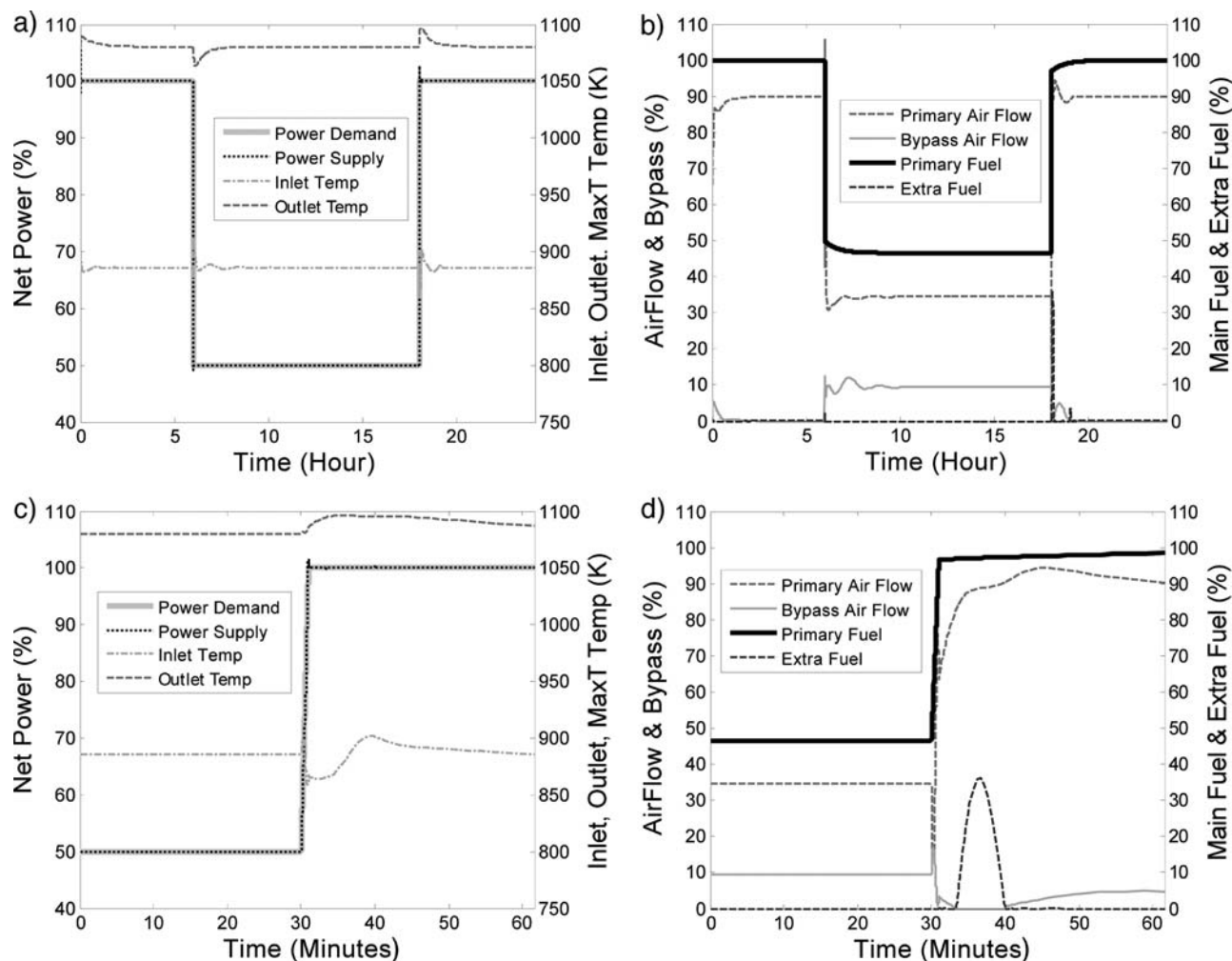
Figure 4. a) 24 hour thermal response to dynamic dispatch with strong feedback controllers. b) Associated 24 hour control response. Zooms of a) and b): c) 30 minute thermal response with strong feedback control. d) Associated 30 min control response.

These cases will be distinguished using the following nomenclature given in Table III. Each case name is comprised of initials representing three specifications: fixed/cyclic power + power density + constraint specification.

The SRU is operated in counter-flow configuration and the inlet anode gas composition corresponds to complete methane conversion in the reformer (99%) and a steam-to-carbon ratio of two. The changes in operating conditions between full and half-load, i.e. system specific

power and possibly air inlet temperature, maximum MEA temperature and fuel utilisation, are applied during the extreme ramps of 1 minute that could be achieved in the system level analyses. Simulations are performed with or without thermal inertia to investigate the effect on the degradation. In the former case, the values for the air ratio at full and half-load are calculated from the degradation analysis without thermal inertia. Table IV lists the operating conditions for the different cases.

Table IV. Operating condition for lifetime durability and degradation tests.

Case	System specific power [W/cm^2]	FC Inlet [K]	Air Ratio[i]	SRU [V][i]	Current density [A/cm^2][i]
a	0.28	973	6.57, 8.10	0.769, 0.634	0.399, 0.496
b	0.28	973	6.57, 8.05	0.769, 0.639	0.399, 0.491
c	0.28	973	6.57, 7.92	0.769, 0.645	0.399, 0.418
d	0.28	973	6.57, 7.98	0.769, 0.646	0.399, 0.485
a	0.14	973	5.50, 5.88	0.841, 0.808	0.180, 0.187
b	0.14	859	3.38, 3.64	0.842, 0.805	0.179, 0.187
c	0.14	913	4.48, 4.83	0.842, 0.805	0.179, 0.188
d	0.14	932	5.35, 5.68	0.812, 0.781	0.186, 0.194
Ref.	0.269	973	6.88	0.738	0.4

[i] (a,b,c,d) Range of values from 0 h to 8000 h. Ref. conditions: values at 1440 h (60 days).

Table V. Relative lifetime extension provided by cycling mode (CP28/14) over constant full power mode (P28), determined by the three lifetime determination methods (see text).

	CP28/14 a	CP28/14 b	CP28/14 c	CP28/14 d
1. Zirconate formation	1.32	1.37	1.35	1.35
2. Decrease of 20% in efficiency	1.21	1.25	1.34	1.30
3. Start of degradation rate higher than −24mV/kh	1.38	1.40	1.42	1.41

Stack Analyses - Determination of Design Limits.— The effect of the maximum MEA temperature on the lifetime is investigated from 1100 K to 1220 K, by steps of 10 K, for a constant system specific power of 0.28 W/cm^2, fuel utilisation of 0.8 and air inlet temperature of 973 K or 950 K. The determination of lifetime was assessed by one of three methods; (i) the activation of the indicator for the formation of zirconate in the LSM-YSZ cathode, i.e. the time at which the formation of such phases is thermodynamically possible, (ii) relative decrease in system efficiency of 20%, (iii) an instantaneous degradation rate of the SRU potential exceeding 24 mV/kh (i.e. approximately 3% / 1000 h), which from experience characterizes the start of a regime of unrecoverable, accelerated degradation.[47]

Table V provides the relative lifetime extensions of the cyclic operation mode over the constant power mode P28, resulting from the three lifetime determination methods. The SRU is set every 60 days at the reference operating point to compare the investigated cases in terms of severity and distribution of the degradation.

Stack Analyses - Degradation Patterns.— Constant system specific power operation produces faster stack degradation than typical constant current endurance tests. Figure 5 depicts the effect of the degradation on the evolution of the SRU potential. The patterns depicted in Figure 5 have been observed in short-stack endurance testing.[47] The model satisfactorily captures the effects of temperature, current density and fuel utilisation without specific adjustment of the model parameters,[33] despite the restriction to five degradation processes, controversy on the underlying mechanisms and simplifications in the modeling approach. Model predictions are also in line with chromium detection post-test analyses.[48] Care is however required when using this model for lifetime predictions, as the dominant degradation

processes may change depending on the materials, stack design and operating strategy. In the conditions studied here, degradation of the electrolyte and anode dominates from approximately 0 h to 2000 h. Degradation mechanisms for the electrolyte and anode reach a plateau after 500–2500 h, and 1000–10000 h, respectively.[33] Chromium contamination of the LSM-YSZ and MIC corrosion dominate degradation beyond this time frame, with chromium contamination acting more severely and leading to accelerated loss of potential. The fixed system specific power with maximum MEA temperature control necessitates ever higher current densities to compensate for the degradation. This effect is compounded by the need for additional power generation to compensate for the increased blower parasitic loss caused by a higher air requirement for cooling as polarization losses increase. The higher current drawn to export the same system power accelerates the degradation (compare dashed/solid grey curves for 0.28 W/cm^2 and 0.4 A/cm^2 in Figure 5). The reduction of the system specific power from 0.28 to 0.14 W/cm^2 increases the lifetime by a factor of approximately 3, because the lower cathode overpotential strongly alleviates chromium contamination.[33] It must be emphasized that for a fixed system output power, more SRUs must be stacked in the case of a lower specific power. Therefore, the benefit is balanced in practice by stacking issues, the gas-tightness of the compartments and extra SRU cost (here ca. double).

The markers in Figure 5 indicate the end of lifetime computed by the three lifetime determination methods. Criterion (i), the formation of zirconates, yields the shortest lifetime estimations, but does not indicate a strict end of service of the stack. Criterion (ii) or (iii), based on a 20% decrease of system efficiency or the start of an accelerated degradation regime, is less stringent. These two methods determine an end of life at potentials lower than 0.65 V, which is below a practical control threshold value. Cycling between 0.28 W/cm^2 and 0.14 W/cm^2 extends the lifetime over operation at 0.28 W/cm^2, mostly since here chromium contamination is alleviated during the phases at half-load. The reasons and benefits of such cyclic operation are discussed in detail further below.

Lower ohmic losses in anode-supported cells allow a reduction of operating temperature, in the view of using lower cost MICs instead of expensive and brittle ceramic interconnectors. Experimental results highlight the predominant influence of the overpotential on the chromium contamination of LSM-YSZ cathodes, rather than current density.[3,4,49] Modeling studies show that for such an electrode, the increase of the operating temperature, with concurrent reduction in cathode overpotential, is an indirect means to extend the lifetime, despite the higher release rate of contaminating species from the MIC.[31] Coatings currently in development are expected to significantly alleviate the limitation caused by the temperature dependence of the oxidation behavior of the MIC, despite the lack of experimental characterizations above 1073 K. Similar to chromium contamination, the temperature has two opposite effects on the risk of formation of zirconate in LSM-YSZ cathodes. Higher operating temperature beneficially reduces the overpotential for a fixed current density, but thermodynamically promotes the formation of the undesirable phase.[6,33]

Figure 6 depicts the lifetime determined by criterion (i, ii, iii) as a function of the maximum MEA temperature. Allowing a higher maximum temperature limit has a beneficial effect over the investigated temperature range, except for the risk of formation of
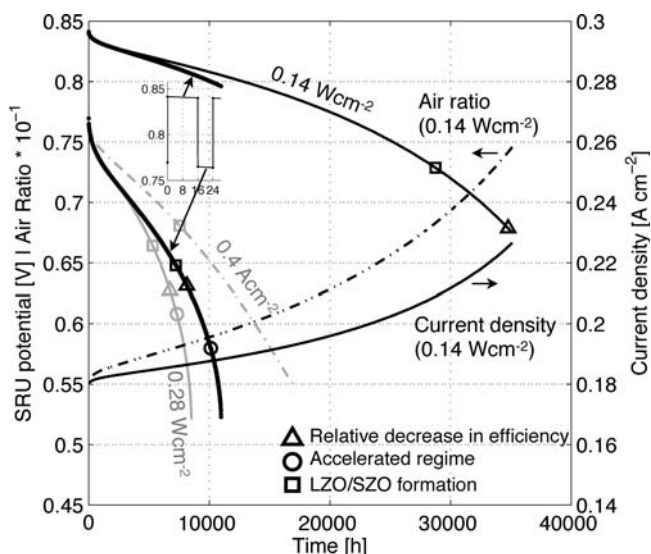
Figure 5. Typical evolution during operation at constant system power of the SRU potential (left), air ratio (left) and current density (right). Case P14 (0.14 W/cm^2), CP28/14a (cycling conditions, details in insert), P28 (0.28 W/cm^2) and operation at a constant current density of 0.4 A cm^{-2}.
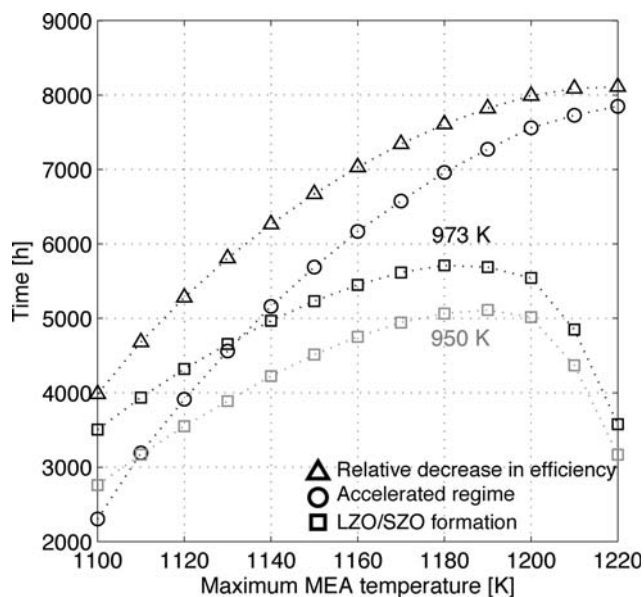
Figure 6. Effect of the maximum MEA temperature on the lifetime, determined by the three criteria. Case P28 (0.28 W/cm^2) with an air inlet temperature of 973 K (black) and 950 K, for the criterion based on the formation of zirconate only (gray).

zirconate, which exhibits a maximum around 1180 K. A lower air inlet temperature of 950 K does not modify this trend. In the conditions studied here, the benefit of a lower air blower parasitic consumption does not compensate the lower electrochemical performance in the colder air inlet zone. This model prediction is comparable to the operating conditions of stacks with electrolyte-supported cells and state-of-the art MIC coating, e.g.[50]

A maximum MEA temperature of 1150 K is used in the following sections, though real systems may exhibit different requirements due to the following considerations: (i) In the case of anode-supported cells, the mechanical compatibility properties of the anode and a possible gadolinia-doped ceria (GDC) cathode buffer layer in the case LSCF cathode is used, along with constraints imposed by the stack thermal management system, limit maximum temperature.[12,31] (ii) The drop in lifetime determined by criterion (i) is more severe at high temperature. In practice, the temperature variation in the stacking direction can be noticeable and is difficult to control due to uneven gas distribution among the stacked repeating units. Thus the constraint must be imposed on the hottest SRU, with all others operating safely below the mechanical limit.

Stack Analyses - Effect of Cycling on Degradation.— Optimization of the operating conditions can maintain the temperature deviation between full-load and half-load within approximately 30 K (case b or c) and 15 K (case d), as shown in Figure 7. Previous results found in literature indicate the possibility of lower deviations. Increased fuel utilization (93%) at half load produces similar overpotentials and thus a nearly identical temperature profile. This case was rejected due to risk of fuel starvation to one or more SRU during transients. As expected, the temperature deviation increases during operation (Figure 7b, 10000 h), because of the redistribution of the current density, governed by the dependence of the degradation phenomena on the local conditions.

Figure 8 depicts the effect of the operation strategy at half-load on the system efficiency and lifetime under fixed and cycled system specific power. At half-load, the lifetime is for all criteria the highest for case P14a. The benefit of a reduced air ratio due to the lower air inlet temperature in case P14b and lower maximum MEA temperature in case P14b do not compensate the detrimental effect on the electrochemical performance. A high fuel utilization of 90% in case
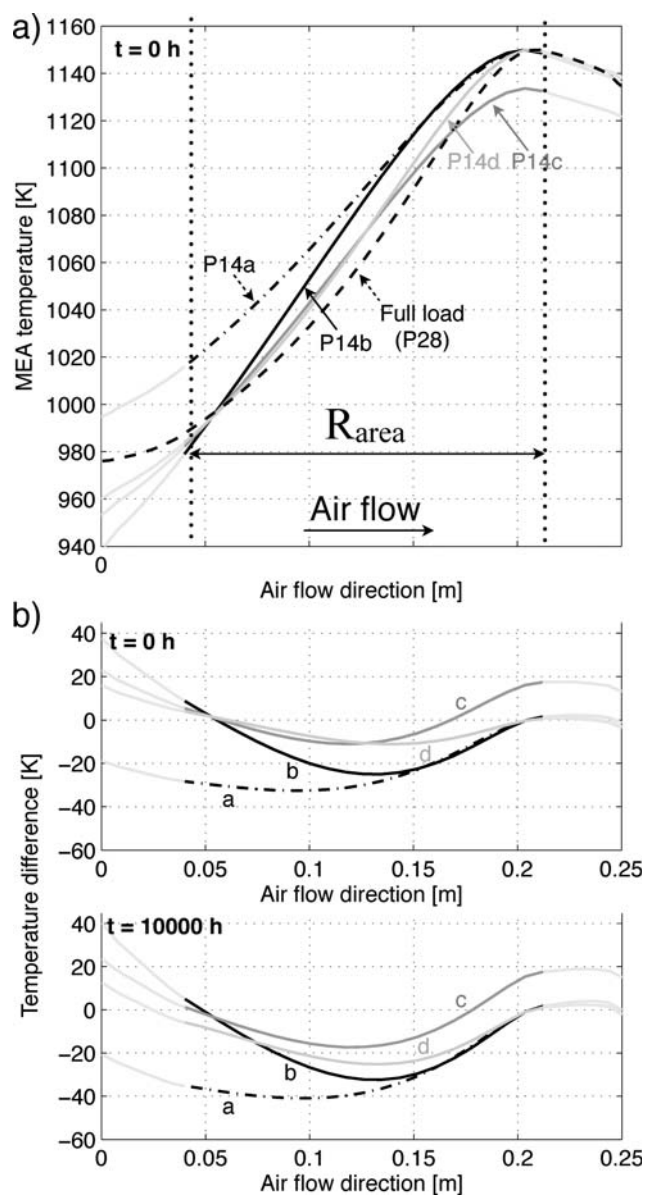

Figure 7. (a) Temperature profiles at the initial time at full load, and part load for the different control cases. (b) Difference between the temperature profile at full load, and part load for the different cases, at the beginning and after 10000 h under cycling condition.

P14d yields a significant increase in system efficiency. Because of the higher air inlet temperature, the time to reach a relative decrease in system efficiency of 20% is delayed, compared with cases P14b and P14c.

In dispatched mode, the difference in degradation behavior between cases does not change at half-load, whereas at full-load, it is affected by the different distribution of the degradation. Case CP28/14a (CP28/14c) yields the shortest (longest) lifetime. Case CP28/14d provides a higher average efficiency along with lifetime extension.

Figure 9 and Figure 10 show the flattening of current density distribution and cathode overpotential under cycling conditions. The fuel utilization of 90% in case CP28/14d confines the domain of high current density close to the fuel inlet. This high current region promotes the formation of zirconate at half-load (Figure 8). In contrast, lower temperature throughout most of the active area at half-load reduces the growth of oxides compared with CP28/14a and CP28/14b
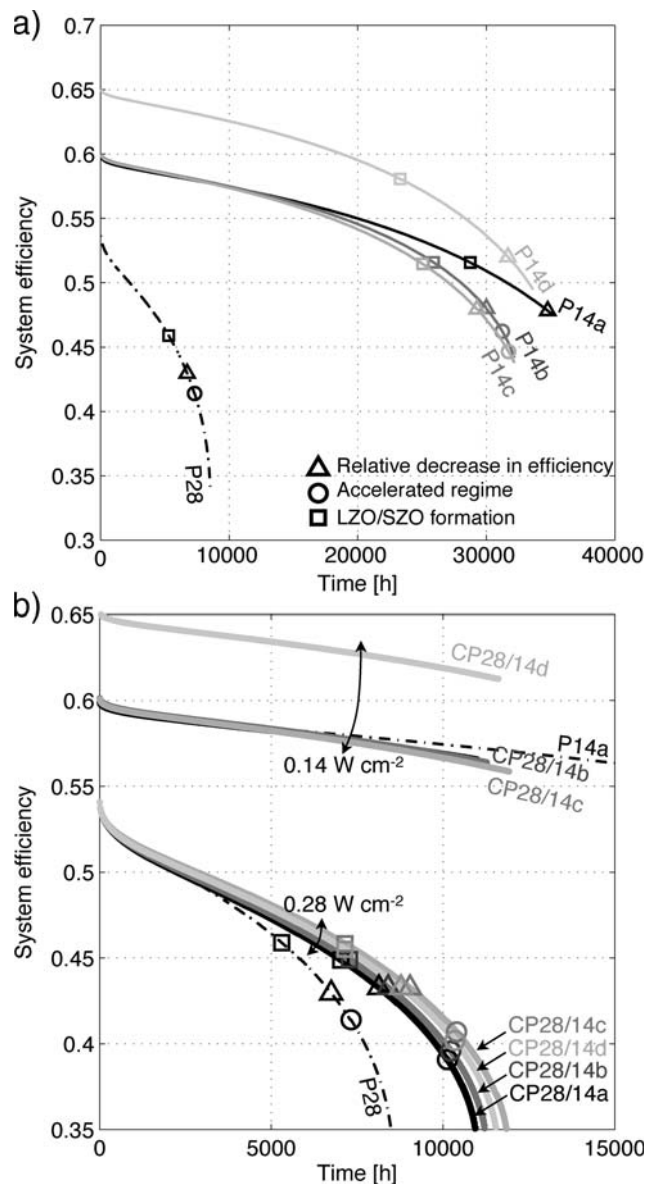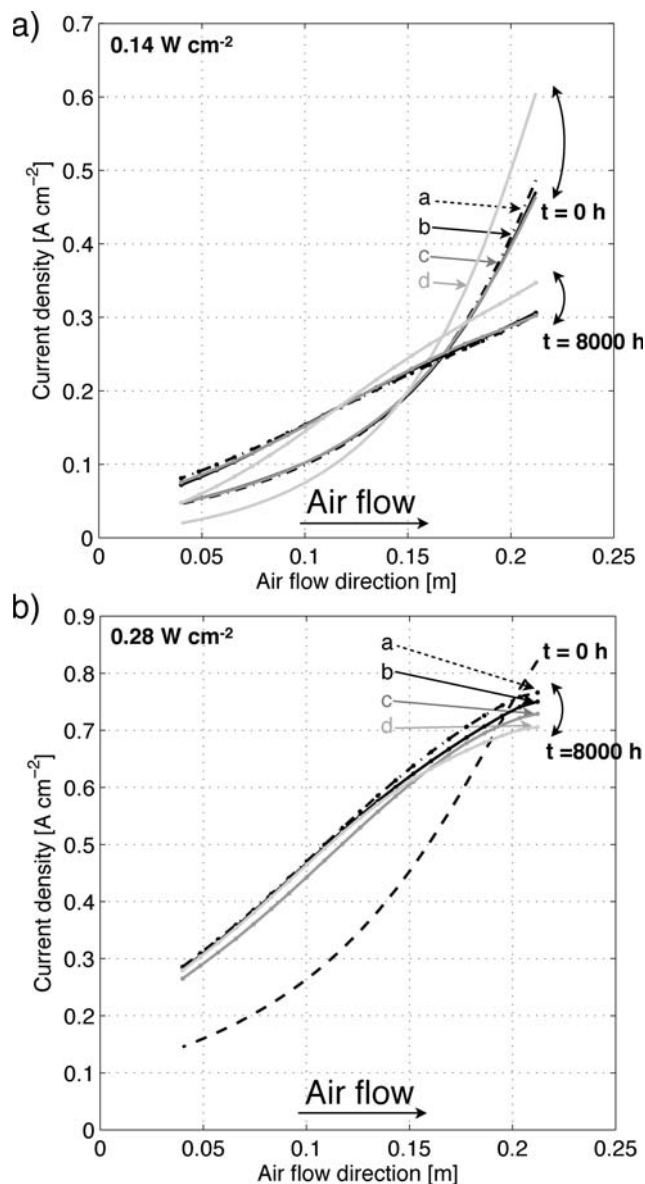
Figure 8. Evolution of the system efficiency during operation at (a) constant system specific power of 0.14 W/cm² (P14a,b,c,d) and 0.28 W/cm² (P28) and (b) during cycling conditions (CP28/14a,b,c,d). The markers indicate the lifetime determined by the three criteria.


Figure 9. Current density profiles at the initial time and after 8000 h of operation under load cycling conditions at part load (a), and full load (b) for the different cases (CP28/14a,b,c,d).

(Figure 7). The reduced oxide growth yields a significant advantage at full-load when the current density increases at the air inlet and chromium contamination occurs at the air outlet where the highest $CrO_2(OH)_{2(g)}$ partial pressure and cathode overpotential are located. Case CP28/14c yields the highest lifetime under cycling conditions because of the same effect of the temperature distribution on the oxidation of the MIC.

During operation, the progressive increase of current density complicates degradation analysis. Figure 11a and 11b depict the evolution of the SRU potential and ASR of the MIC and of the cathode at the reference conditions. The degradation of the cathode induces higher degradation during constant load operation. In contrast, the evolution of the ASR of the MIC and electrolyte (not depicted) depends solely on the temperature profile and its history. The slight modification of the oxidation of the MIC by the different half-load conditions causes differences in degradation behavior (compare CP28/14a and CP28/14c). In cases P14 (not displayed in Figure 11), the evolutions

of the SRU potential and ASR of the cathode and the MIC at the reference condition are identical to those displayed in Figure 11 during the first 15000 h at a constant system specific power (not depicted). In the longer-term, the trends change in accordance with the results shown in Figure 8. This highlights the crucial importance of the history on the degradation behavior of a SOFC stack.
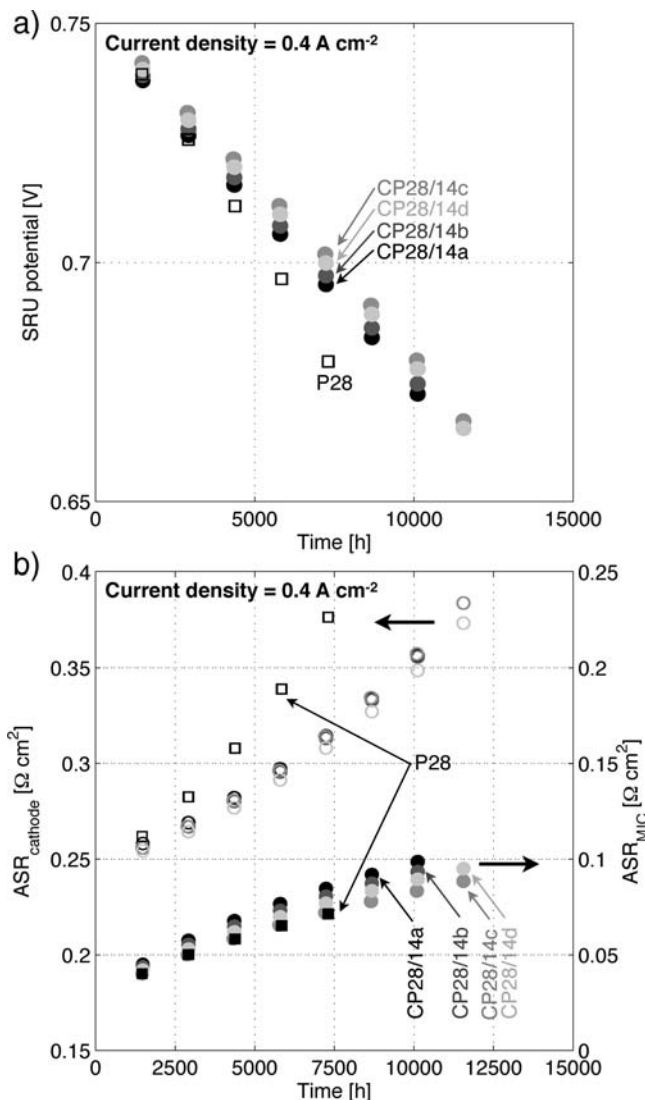
The implementation of thermal inertia in the model marginally modifies the lifetime predictions. The evolution of the system efficiency and SRU potential are almost identical. Figure 12 shows the maximum and minimum MEA temperature and chromium deposition rate qualitatively compensating during changes between full- and half-load. Significant variations occur within short time periods, in the range of 3 h per day. The most notable detrimental effect of transient is on the time before the start of formation of zirconate, which occurs approximately 100 h earlier (not depicted).

The simulated ramp-up and turn-down between full- and half power performed in 1 min could cause immediate or delayed mechanical failure, because of sudden changes in stress fields. The
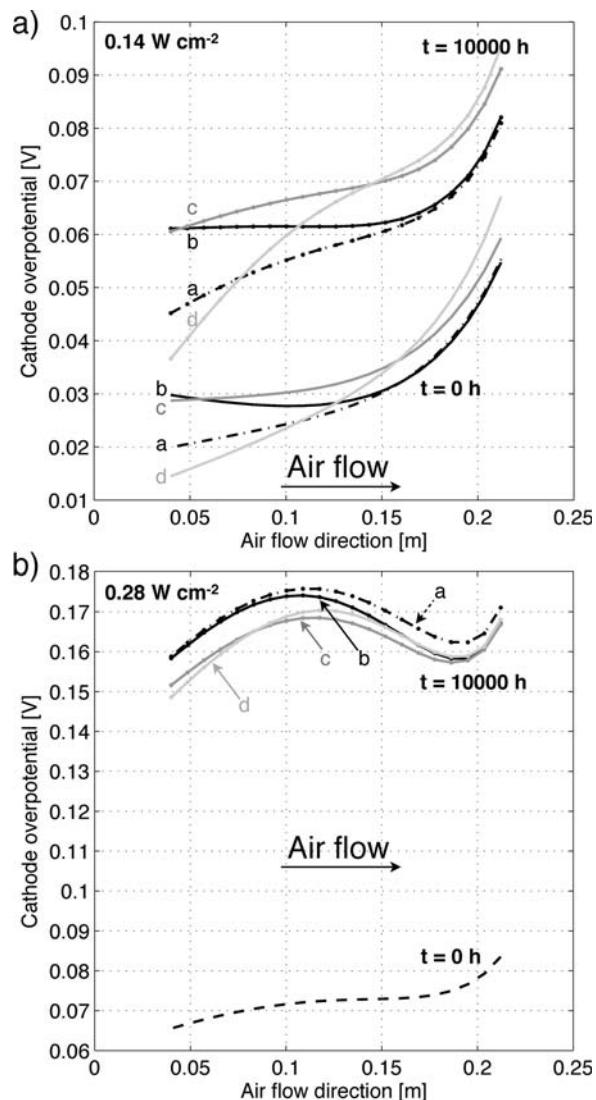
Figure 10. Distribution of the cathode overpotential during cycling conditions (CP28/14a,b,c,d) at the initial time and 10000 h, at (a) 0.14 W/cm² and (b) 0.28 W/cm².

Figure 11. Evolution at the reference conditions (every 60 days or 1440 h) of a) the SRU potential and b) the ASR of the cathode (left axis) and MIC (right axis) during operation under dispatched operation (circles: CP28/14a,b,c,d) and constant system specific power (squares: P28).

present modeling tools have been combined to a contact finite-element SRU model for structural analysis. The results are presented elsewhere.[15,16,31] The models predict a significant increase in the risks of cell cracking, MIC thermal buckling and loss of gas-tightness of the compartments during transients, in the case of unsuited control strategy.[15,16] In the longer term, the mitigation of electrochemical degradation and mechanical reliability and durability place different requirements on the operating conditions.[31] The uneven distributions of electrochemical performance degradation, irreversible deformation and alterations of the mechanical properties of the materials generated under given operating conditions induce a history-dependent behavior. This increases the risks of mechanical failure if the conditions are changed, such as during electrical power demand tracking, idling or thermal cycling. Further investigations are required to confirm that the spatial temperature control applied in the present study can alleviate many of these issues, as is anticipated. Experimental validations at the stack and system levels are needed to verify the capability of the models to predict reliably the system and stack degradation behavior in dynamic dispatch mode. At the stack/SRU scale, segmented-cell endurance tests performed under cycling conditions with spatial temperature control can serve for a detailed verification of the model predictions for one SOFC stack instance. Such tests could provide access to the distribution of the electrochemical degradation, induced by interactions between the different processes at the cell and SRU scale. Post-test analyses can further provide the relationship between local conditions, electrochemical degradation and physico-chemical alterations of the materials.

Economic analysis.— The market share of fuel cells for distributed power is growing rapidly. Widespread deployment without government incentives will target markets with the potential for rapid return on investment (ROI). Southern California with its high electrical prices, low natural gas prices, and strict emissions regulations is a natural market for SOFC technology. The aim of SOFC dispatching is to produce a greater portion of the lifetime energy (kWh) during more highly valued times. By shifting production to periods of peak electricity pricing, producer/consumers can offset a larger portion of their electrical cost.

Table VI lists the Southern California Edison's time of use (TOU) electricity pricing, methane and SOFC stack price to integrate degradation simulations with economic analysis. The power demand is assumed to follow the simplified pattern used for degradation

Table VI. Southern California Edison's time of use (TOU) electricity pricing, methane and SOFC stack price for economic analysis. Annual saving with respect to the case where all the electricity demand is supplied from the grid for three SOFC system operation strategies (P14d, CP28/14d, P28), along with averaged system efficiency over the lifetime, determined by a decrease of 20% in system efficiency and annual saving.

	0–8 AM	8–12 AM	12–18 AM	18–21 AM	21–23 AM	23–24 AM
Pricing A[a]	0.103	0.171	0.304	0.171	0.155	0.103
Pricing B[b]	0.105	0.137	0.167	0.137	0.121	0.105
	Stack maximum power (kW)	Price of methane ($/therm)	Stack price ($/kW)	Lifetime for economic analysis	Averaged efficiency	Annual saving
P14d	10	1	500	10	0.599	10%
CP28/14d	20	1	500	2.6	0.583	28%
P28	20	1	500	2	0.483	6%

[a] Pricing is for light industrial with some local generation ($/kWh/month).
[b] Pricing for no onsite generation ($/kWh/month).

analysis. For the purpose of the economic analysis, lifetime for the P28 base case is allowed to reach 2 years, roughly twice as long as displayed in Figure 5. Correspondingly, lifetime for the other cases (P14 and CP28/14) is accordingly extended. Three scenarii with a same stack are compared: (i) all the electricity is supplied from

Figure 12. (a) Evolution of the MEA temperature at location A (right axis) and location B (left axis), during the cycling. (b) Evolution of the averaged deposition rate of chromium at the active sites in the cathode. Simulations with thermal inertia, location A and B are indicated in Figure 1.

grid (Schedule B pricing) (ii) a SOFC system is operated in mode P14d (10 kW) and the peak power is supplied from grid (Schedule A pricing) (iii) a SOFC system is operated in dispatch mode CP14/28d to track the power demand (Schedule A pricing) (iv) a SOFC system is operated in mode CP28 (20 kW) and the excess power during night time is exported to the grid. (Schedule A pricing with additional 50% value for exported electricity). Strategies P14d and CP28/14d are used for comparison, since they provide the highest economical advantages among the constant system power output and dispatch power mode, respectively, because of the higher efficiency.

Economic analysis allows to balance lifetime, produced energy and power demand tracking capabilities. It shows that a greater ROI can be achieved with dispatched SOFC system operation. Light industrial consumers subscribing to TOU pricing could save 28% annually with current gas prices and a dynamically dispatched FC (CP28/14d). Without government incentives or an interconnect agreement a base SOFC system could save up to 10% annually (P14). With an interconnect agreement allowing export of excess power a base loaded SOFC system could save up to 6% annually. Combined heat and power applications can further improve the ROI and shorten the payback period for each of these deployment strategies when the waste heat can be effectively utilized and valued.

Conclusions

The outcome of combining complete system level and SRU/stack degradation models to analyze the effects of dynamic dispatch on the lifetime of a SOFC system is presented. Constant system power output and diurnal dynamic dispatch modes have been investigated. The system level analysis showed that an improperly controlled system will exceed thermal limits during transient operation, but properly calibrated control systems can minimize fluctuations to just a few degrees. A minimum of six independent actuators were needed to fully control the SOFC system behavior during transient operation. However, each actuator represents a physical device thus making the control system applicable to a realistic physical system. The coupled nature of the electrochemical and physical systems leads to complex dynamic interactions that warrant further investigation.

The thermal inertia of the system first led to an oscillatory behavior during turn-down which, if left unaccounted for, will damage the system. The thermal oscillations were mitigated with system control development to acceptable amplitude and completely damped within 30 minutes of the system transient. It is feasible that further control development could further improve the thermal response of the integrated system. Spatial resolution of the SRU temperature profile reveals gradient fluctuations less severe than anticipated. The mass of the electrochemical system induces thermal transients at a very long scale that are mitigated by a robust control scheme.

These results have been used as operating conditions for degradation simulations with a dedicated SRU model. The predicted degradation behavior is qualitatively in line with experimental results
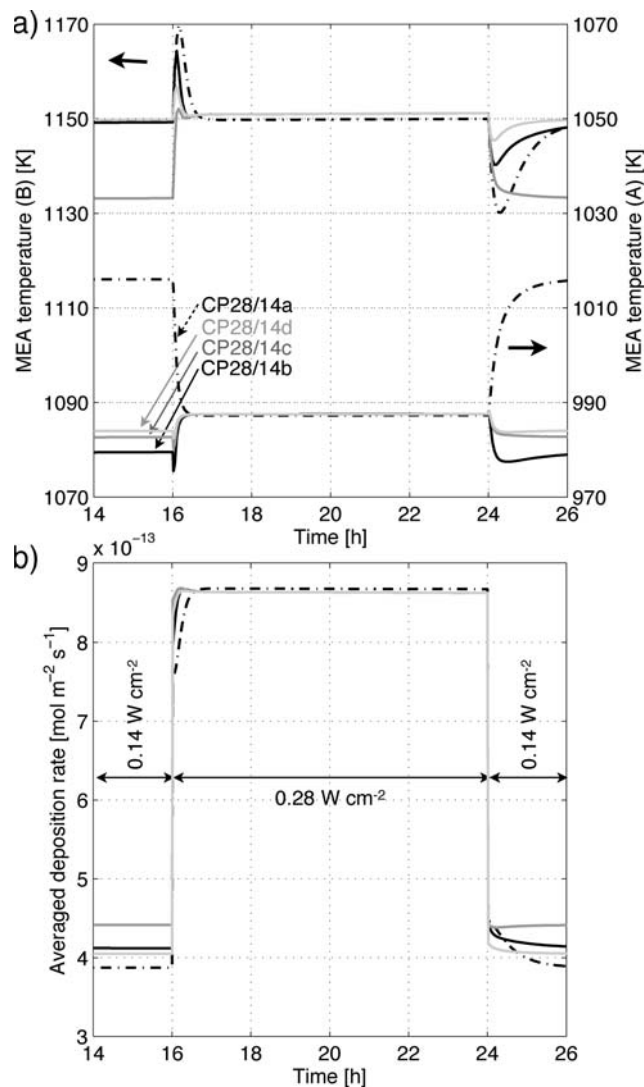
from the literature. The cyclic dispatch mode yielded an extension of the lifetime by a factor up to 1.40, compared with the constant full-load operating mode. The decrease of the cathode overpotential produced by an increase of the maximum MEA temperature alleviates the chromium contamination of the LSM-YSZ cathode, despite the higher release rate of volatile chromium species from the MICs. In the conditions studied here, the risk of formation of zirconate in the LSM-YSZ cathode limits the maximum MEA temperature to 1180 K.

The four strategies for system control at half-load operation yield differing effects upon the lifetime for constant half-power and cyclic dispatch modes. The local accumulation of the degradation induced by MIC oxidation and chromium contamination of the cathode differs between fixed operation and dispatch mode. For the cyclic dispatch mode the strategy of reducing the maximum MEA temperature at half-load (case c) yielded the greatest lifetime extension, whereas the strategy of increasing fuel utilization from 0.8 to 0.9 (case d) enabled higher system efficiency with minimal detrimental effect on lifetime.

The electrical energy produced during the lifetime of the SOFC device, and the efficiency at which it is delivered, is highest in the constant half-power mode, second highest in dynamic dispatch mode, and lowest at full-load operation. Economic analysis to balance these aspects shows that light industrial consumers subscribing to TOU pricing could save 28% annually with current gas prices and a dynamically dispatched FC (CP28/14d). Without government incentives or an interconnect agreement a base SOFC system could save up to 10% annually (P14). With an interconnect agreement allowing exportation of excess power a base loaded SOFC system could save up to 6% annually.

The present simulation results are encouraging to explore further the operation envelope of SOFC systems and understand where the limits are. Dedicated structural analyses and experimental validations at the system level will be needed to ascertain their suitability for cost-efficient load following.

Nomenclature

Latin letters

A	area (m^2)
C_p	specific heat capacity at constant pressure (J K^{-1} kg^{-1})
c_R^*	catalyst layer reactant concentration (mol m^{-3})
c_R^0	bulk reactant concentration (mol m^{-3})
D_{ij}^{eff}	effective diffusion coefficient (m^2 s^{-1})
F	Faraday constant (C mol^{-1})
ΔG_{act}	change in Gibbs free energy (J mol^{-1})
j, j_L	current density, limiting current density (A m^{-2})
K	(K Ω^{-1} m^{-1})
m	mass of solids (kg)
$\dot{n}$	molar flow rate (mol s^{-1})
$\dot{N}$	molar flow rate (mol s^{-1})
P	pressure (Pa)
Q_i	heat transfer rates between control volumes (J s^{-1})
$\dot{q}$	heat generation within control volume (J s^{-1})
R_U	gas constant (J mol^{-1} K^{-1})
$R_{Ref+consume}$	net reaction vector (kmol/s)
t	thickness (m)
T	temperature (K)
$\forall$	volume (m^3)
$\dot{W}$	power (W)
$x_{O_2\|d}$	molar fraction of O$_2$
X_i	species mole fraction

Greek letters

A	symmetry coefficient
η	overpotential (V)

Indice

act	activation
an	anode
cath	cathode
in	control volume inlet
out	control volume outlet
ohm	ohmic

Superscript

c	cathode
M	membrane

Acronym

FC	fuel cell
GDC	gadolinia-doped ceria
LSCF	lanthanum strontium cobaltite ferrite
LSM	lanthanum strontium manganite
LZO	lanthanum zirconate
MEA	membrane electrode assembly
MIC	metallic interconnect
Ni-YSZ	anode
ROI	return on investment
SRU	single repeating unit
SZO	strontium zirconate
TOU	time of use
TPB	triple-phase boundary
YSZ	yttria-stabilised zirconia
BoP	balance of plant

References

1. T. Horita, K. Yamaji, H. Yokokawa, A. Toji, T. Uehara, K. Ogasawara, H. Kameda, Y. Matsuzaki, and S. Yamashita. *Int. J. of Hydrogen Energy*, **33**, 6308 B (2008).
2. T. Horita, K. Yamaji, Y. Xiong, H. Kishimoto, N. Sakai, and H. Yokokawa. *Solid State Ionics*, **175**, 157 (2004).
3. E. Konysheva, J. Mertens, H. Penkalla, L. Singheiser, and K. Hilpert, *J. Electrochem. Soc.*, **154**, B1252 (2007).
4. S. Jiang, J. P. Zhang, L. Apateanu, and K. Foger *J. Electrochem. Soc.*, **147**, 4013 (2000).
5. A. Hagen, Y. Liu, R. Barfod, and P. Hendriksen, *J. Electrochem. Soc.*, **155**, B1047 (2008).
6. Y. Liu, A. Hagen, R. Barfod, M. Chen, H. Wang, F. Poulsen, and P. Hendriksen, *Solid State Ionics*, **180**, 1298 (2009).
7. A. Faes, A. Hessler-Wyser, D. Presvytes, C. Vayenas, and J. Van herle, *Fuel Cells*, **9**, 6 (2009).
8. D. Simwonis, F. Tietz, and D. Stöver, *Solid State Ionics*, **132**, 241 (2000).
9. C. Haering, A. Roosen, and H. Schichl, *Solid State Ionics*, **176**, 253 (2005).
10. J. Kondoh, T. Kawashima, S. Kikuchi, Y. Tomii, and Y. Ito, *J. Electrochem. Soc.*, **145**, 1527 (1998).
11. B. Sun, R. Rudkin, and A. Atkinson. *Fuel Cells* **9** (6): 805–813 (2009).
12. A. Nakajo, J. Van herle, and D. Favrat. *Fuel Cells*, **11**(4), 537, (2011).
13. J. Laurencin, G. Delette, F. Lefebvre-Joud, and M. Dupeux. *J. European Ceramic Society*, **28**(9):1857–1869, 2008.
14. C.-K. Lin, T.-T. Chen, Y.-P. Chyou, and L.-K. Chiang. *J. Power Sources*, **164**(1):238–251, 2007.
15. A. Nakajo, Z. Wuillemin, J. V. herle, and D. Favrat. *J. Power Sources*, **193**(1):203–215, 2009.
16. A. Nakajo, Z. Wuillemin, J. V. herle, and D. Favrat. *J. Power Sources*, **193** (1):216–226, 2009.
17. N. Govindaraju, W. Liu, X. Sun, P. Singh, and R. Singh. *J. Power Sources*, **190**(2):476–484, 2009.
18. M. Fardadi, F. Mueller, and F. Jabbari, *J. Power Sources*, **195**(13):4222–4233, 2010.
19. J. Brouwer, F. Jabbari, E. Martins Leal, and T. Orr, *J. Power Sources*, **158**, 213 (2005).
20. T. Kaneko, J. Brouwer, and G. S. Samuelsen, *J. Power Sources*, **160**, 316 (2006).
21. D. McLarty, J. Brouwer, and G. S. Samuelsen, *ASME Paper # FuelCell2010-33329*, (2010).
22. F. Mueller, University of California, Irvine, Master's thesis (2005).
23. R. Roberts, J. Brouwer, F. Jabbari, T. Junker, and H. Ghezel-Ayagh, *J. Power Sources*, **161**, 484 (2006).
24. R. Roberts, and J. Brouwer, *J. Fuel Cell Science and Tech.*, **3**, 18 (2006).
25. R. Roberts, University of California, Irvine, PhD thesis (2005).

26. F. Mueller, J. Brouwer, F. Jabbari, and S. Samuelsen. *Journal of Fuel Cell Science and Technology*, **3**, 2 (2006).
27. Y. Kuniba. University of California, Irvine, PhD thesis (2007).
28. F. Mueller, F. Jabbari, J. Brouwer, S. T. Junker, and H. Ghezel-Ayagh, *J. Dynamic Systems, Measurement, and Control*, **131**, 051002 (2009).
29. F. Mueller, University of California, Irvine, PhD thesis 2008.
30. F. Mueller, R. Gaynor, A. Auld, J. Brouwer, F. Jabbari, and G. S. Samuelsen, *J. Power Sources*, **176**, 229 (2008).
31. A. Nakajo. Ecole Polytechnique Fédérale de Lausanne, PhD thesis 4930 (2011).
32. A. Nakajo, Z. Wuillemin, P. Metzger, S. Diethelm, G. Schiller, J. Van herle, and D. Favrat, *J. Electrochem. Soc.*, **158** (9), B1083–B1101, 2011.
33. A. Nakajo, P. Tanasini, J. Van herle, and D. Favrat, *J. Electrochem. Soc.*, **158** (9):B1102–B1118, 2011.
34. J. Xu and G. Froment, *AIChE Journal*, **35**, 88 (1989).
35. F. Mueller, J. Brouwer, S. Kang, H-S. Kim, and K. D. Min, *J. Power Sources*, **163**, 814 (2007).
36. Process Systems Enterprise Ltd. gPROMS, London.
37. F. Bouwmeester, H. van Heuveln, and H. J. M., *J. Electrochem. Soc.*, **144**, 134 (1997).
38. A. Achenbach and E. Riensche, *J. Power Sources*, **52**, 283 (1994).
39. H. Zhu, R. J. Kee, V. M. Janardhanan, O. Deutschmann, and D. G. Goodwin, *J. Electrochem. Soc.*, **152**, A2427 (2005).
40. J. Froitzheim, G. Meier, L. Niewolak, P. Ennis, H. Hattendorf, L. Singheiser, and W. Quadakkers, *J. Power Sources*, **178**, 163 (2008).
41. W. Liu, X. Sun, E. Stephens, and M. Khaleel, *J. Power Sources*, **189**, 1044 (2009).
42. E. Opila, N. Jacobson, D. Myers, and E. Copland. *J. Minerals, Metals and Materials Soc.*, **58**, 22 (2006).
43. Z. Wuillemin. Ecole Polytechnique Fédérale de Lausanne, PhD thesis 4525, (2009).
44. B. Ebbinghaus, *Combust. and Flame*, **93**, 119 (1993).
45. G. R. Holcomb and D. E. Alman *Scripta Materialia*, **54**, 1821 (2006).
46. M. Stanislowski, E. Wessel, K. Hilpert, T. Markus, and L. Singheiser. *J. Electrochem. Soc.*, **154**, A295 (2007).
47. L. de Haart, J. Mougin, O. Posdziech, J. Kiviaho, and N. Menzler. *Fuel Cells*, **9**, 794 (2009).
48. A. J. Schuler, Z. Wuillemin, A. Hessler-Wyser, C. Ludwig, and J. Van herle, *ECS Trans.*, **35** (1), 2001 (2011).
49. J. A. Schuler, P. Tanasini, A. Hessler-Wyser, and J. Van herle, *Scripta Materialia*, **63**, 895 (2010).
50. A. Mai, B. Iwanschitz, R. Denzler, D. Haberstock, and A. Schuler, In *Proceedings of the 9th European Fuel Cell Forum*, A706 (2010).